

H₂CO and H110 α Observations toward the Aquila Molecular Cloud

TOKTARKHAN KOMESH,^{1,2,3} JARKEN ESIMBEK,^{1,4} WILLEM BAAN,^{1,5} JIANJUN ZHOU,^{1,4} DALEI LI,^{1,4} GANG WU,^{1,4}
YUXIN HE,^{1,4} SERIKBEK SAILANBEK,^{1,2,3} XINDI TANG,^{1,4} AND ARAILYM MANAPBAYEVA²

¹*Xinjiang Astronomical Observatory, Chinese Academy of Sciences, Urumqi 830011, PR China*

²*Department of Solid State Physics and Nonlinear Physics, Faculty of Physics and Technology, Al-Farabi Kazakh National University, Almaty, 050040, Kazakhstan*

³*University of the Chinese Academy of Sciences, Beijing 100080, P. R. China*

⁴*Key Laboratory of Radio Astronomy, Chinese Academy of Sciences, Urumqi 830011, PR China*

⁵*Netherlands Institute for Radio Astronomy, ASTRON, 7991 PD, Dwingeloo, The Netherlands*

ABSTRACT

The formaldehyde H₂CO(1₁₀ – 1₁₁) absorption line and H110 α radio recombination line (RRL) have been observed toward the Aquila Molecular Cloud using the Nanshan 25 m telescope operated by the Xinjiang Astronomical Observatory CAS. These first observations of the H₂CO (1₁₀ – 1₁₁) absorption line determine the extent of the molecular regions that are affected by the ongoing star formation in the Aquila molecular complex and show some of the dynamic properties. The distribution of the excitation temperature T_{ex} for H₂CO identifies the two known star formation regions W40 and Serpens South as well as a smaller new region Serpens 3. The intensity and velocity distributions of H₂CO and ¹³CO(1 – 0) do not agree well with each other, which confirms that the H₂CO absorption structure is mostly determined by the excitation of the molecules resulting from the star formation rather than by the availability of molecular material as represented by the distribution. Some velocity-coherent linear ¹³CO(1 – 0) structures have been identified in velocity channel maps of H₂CO and it is found that the three star formation regions lie on the intersect points of filaments. The H110 α emission is found only at the location of the W40 H II region and spectral profile indicates a redshifted spherical outflow structure in the outskirts of the H II region. Sensitive mapping of H₂CO absorption of the Aquila Complex has correctly identified the locations of star-formation activity in complex molecular clouds and the spectral profiles reveal the dominant velocity components and may identify the presence of outflows.

Keywords: Molecular clouds — ISM: molecules — stars: formation

1. INTRODUCTION

The Aquila Molecular Cloud (AMC) or the Aquila Rift complex is located along the Galactic plane and stretches from 20° to 40° in longitude and from -1° to 10° in latitude, as revealed by CO and HI, observations (Dame et al. 2001; Prato et al. 2008). The western part of Aquila Rift contains several active star-forming regions: Serpens Main, Serpens South, W40, and MWC 297. Here, we focus on part of the Aquila Rift complex that harbors two known sites of star formation: the western Serpens South is a young embedded cluster

(Bontemps et al. 2010), and the eastern W40 is a cluster associated with an H II region (Smith et al. 1985).

Spitzer observations show W40 and the embedded cluster Serpens South nearby on the sky such that Serpens South and is seemingly part of the W40 region (Gutermuth et al. 2008). The distance to Serpens Main and W40 has recently been measured to be 436 pc and the distance to Serpens South should be similar, because the velocities of these clouds are very similar (Ortiz-León et al. 2017). Similarly Shimoikura et al. (2018) proposed that Serpens South region may be interacting with the W40 HII expanding shell, which would place Serpens South and W40 at almost the same distance. However, wide-field observations of the ¹²CO (2 – 1) and ¹³CO (2 – 1) emissions towards the Aquila Rift show the two spatially-extended components Serpens South and W40 at different velocities,

which suggests that arcs and large-scale expanding bubbles and/or flows affect the velocity fields and play a role in the formation and evolution of these clouds (Nakamura et al. 2017).

In this study we consider the H_2CO absorption at 4.830 GHz and $\text{H}110\alpha$ recombination line emission at 4.874 GHz in the Aquila Rift. The distribution of H_2CO absorption in the Galaxy and against 262 Galactic radio sources has been surveyed showing that H_2CO absorption is associated with most of the H II regions (Davies & Few 1979; Downes et al. 1980; Pipenbrink & Wendker 1988). Since H_2CO is only seen in absorption against a background continuum it only samples the physical conditions in the foreground of the H II region, while other mm and sub-mm spectral lines are observed both in front and behind the source. The correlation between the distribution of ^{13}CO emission and H_2CO absorption is found to be very strong such that both components arise from similar regions (Tang et al. 2013).

In the present paper, we show results of the first H_2CO and $\text{H}110\alpha$ observations toward the W40 and Serpens South regions of the Aquila Rift. In Section 2, we present the details of our observations. The results and discussion of the observations are described in Section 3. Finally, the conclusions are summarised in Section 4.

2. OBSERVATIONS AND DATABASE ARCHIVES

2.1. H_2CO and $\text{H}110\alpha$ observations

The H_2CO (1_{10-111}) absorption line ($\lambda = 6$ cm, $\nu_0 = 4829.6594$ MHz) and the $\text{H}110\alpha$ RRL ($\nu_0 = 4874.1570$ MHz) have been observed in the Aquila molecular cloud during February 2015 using the Nanshan 25-m radio telescope of the Xinjiang Astronomical Observatory of Chinese Academy of Sciences. The 25-m radio telescope has an HPBW (half power beam width) of $10'$ at this wavelength. The observations were performed in an On-The-Fly mode with an average integration time of one minute for each position. The central position of the observing pattern is $18^h30^m03^s -2^{\circ}02'40''$ (J2000). The 6 cm low noise receiver had a system temperature of about 23 K during the observations. In order to observe the H_2CO and the $\text{H}110\alpha$ RR lines simultaneously, the center frequency of the spectrometer was set at 4851.9102 MHz. A Digital Filter Bank was used with 8192 channels and 64 MHz bandwidth, corresponding to a velocity resolution of 0.48 km s^{-1} at 4.852 GHz. The sensitivity of the system (DPFU, Degrees Per Flux Unit) was 0.116 K Jy^{-1} and the main beam efficiency at this wavelength is 65%.

We used CLASS and GREG (parts of GILDAS) to process the H_2CO and $\text{H}110\alpha$ line data. The area of the

Aquila molecular cloud observed is $100' \times 100'$. The average sigma noise level of these maps is 0.020 K. The signal to noise ratio of all detected points was better than 3. Assuming a distance of 436 pc for the Aquila complex, the spatial scale of the maps is 0.124 pc arcmin^{-1} .

2.2. Archival data

The $^{13}\text{CO}(1-0)$ and $^{12}\text{CO}(1-0)$ data observed with the 13.7 m millimeter wave telescope of Purple Mountain Observatory in Delingha in April and May 2011 have been taken from the Millimeter Wave Radio Astronomy Database¹. The velocity resolution of this data is 0.17 km s^{-1} and the system temperature of these on-the-fly mode observations ranged from 250 to 310 K. The $^{13}\text{CO}(J = 1-0)$ data to $10'$ has been resampled onto the H_2CO observing grid. The sigma noise levels of the $^{13}\text{CO}(1-0)$ and $^{12}\text{CO}(1-0)$ data are 0.056 K and 0.122 K, respectively. The 6 cm continuum data for the Aquila Rift region has been obtained from the Sino-German $\lambda 6$ polarization survey of the Galactic Plane using the Urumqi 25 m telescope of the National Astronomical Observatories, CAS, were taken by Sun et al. (2011). The central frequency of the data was 4.8 GHz, and the observing bandwidth was 600 MHz. The resolution of the data is $9.5'$ and the system temperature was about 22 K at the zenith.

3. RESULTS AND DISCUSSION

3.1. The Formaldehyde Absorption

The intensity map of the H_2CO absorption towards the Aquila Molecular Cloud integrated over the velocity interval of 3 - 11 km s^{-1} is shown in Fig.1a. The observation parameters are shown in Tab.1. Two concentrations can be seen in the map, that correspond to the W40 H II region and Serpens South with maximum flux values of the H_2CO absorption of -1.097 K km s^{-1} and -1.007 K km s^{-1} . The velocities at the offsets of (20,-5) and (0,0) are 7.125 km s^{-1} and 6.216 km s^{-1} , respectively. The color-scale map of the $^{13}\text{CO}(J = 1-0)$ emission is shown together with the H_2CO contours in Fig.1b. The ^{13}CO emission map at Serpens South shows several elongated structures that only partially follow the H_2CO absorption structure and there is enhanced emission on the north side of W40 that could result from heating by the H II region.

The H_2CO absorption and the ^{13}CO emission structures are not in good agreement with each other in both the Serpens South and the H II region. The ^{13}CO emission at W40 is offset and there is no clear concentration

¹ <http://www.radioast.nsd.c.cn>

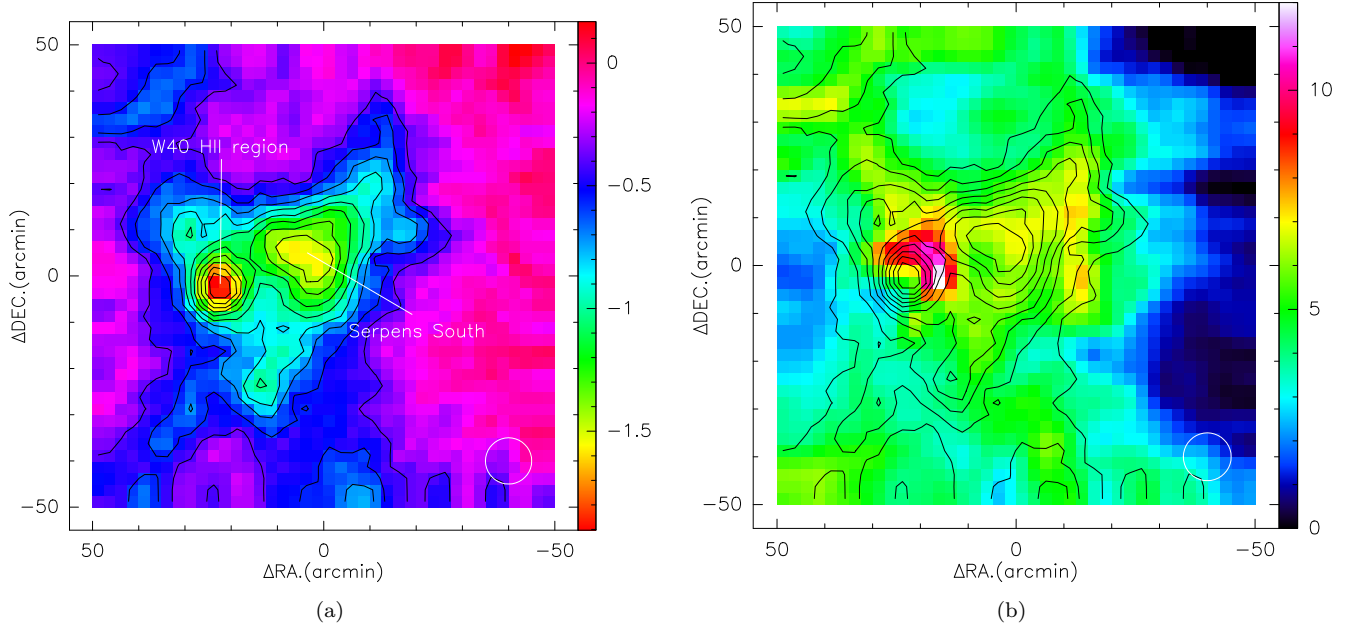


Figure 1. (a) A map of the integrated intensities of H₂CO absorption line and (b) a map of the ¹³CO(J = 1 – 0) integrated intensity superposed on contours of H₂CO toward Aquila molecular cloud. The color bars are given in units of K km s⁻¹. Contour levels of the H₂CO intensity map are -0.4 to -1.8 in steps of -0.15 K km s⁻¹ for both panels. White circles in the lower right illustrate the half-power beam size of 10'.

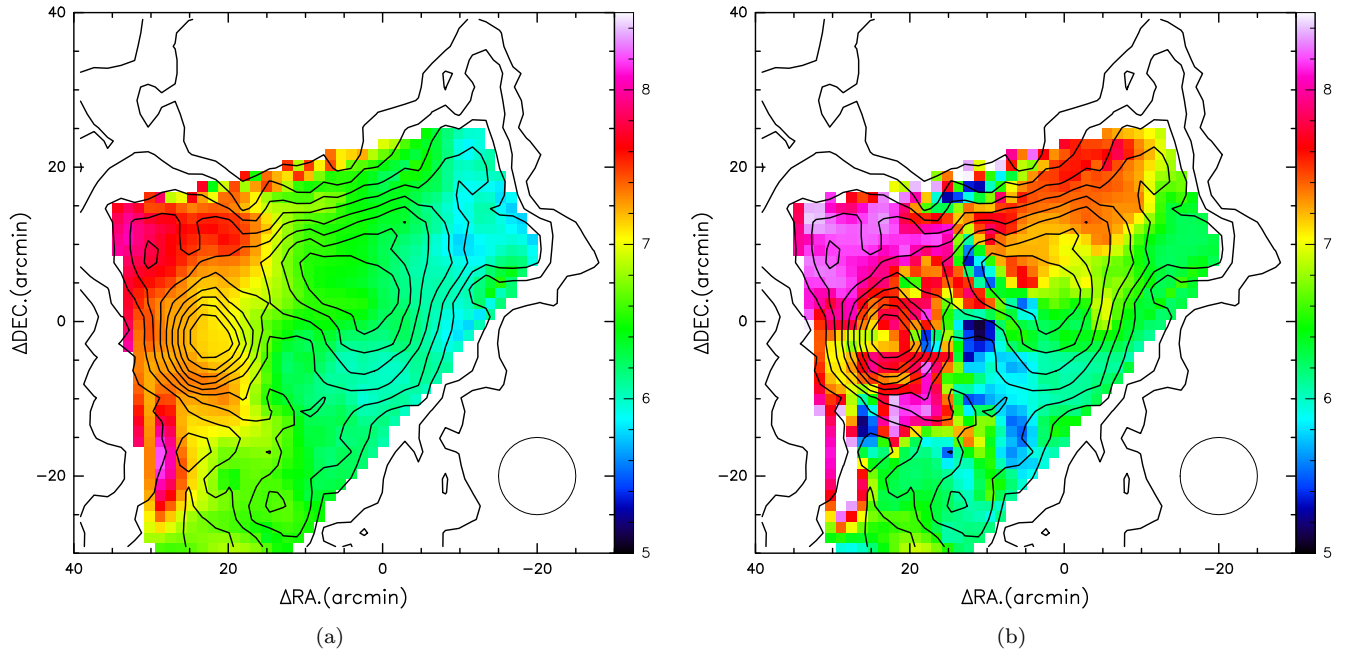


Figure 2. (a) The distribution of the centroid velocity of the H₂CO absorption and (b) of the ¹³CO(1 – 0) emission superposed on the integrated intensity contours of H₂CO. The colour bars are given in units of km s⁻¹. The H₂CO contour levels are the same as those in Fig.1. Black circles in the lower right illustrate the half-power beam size of 10'.

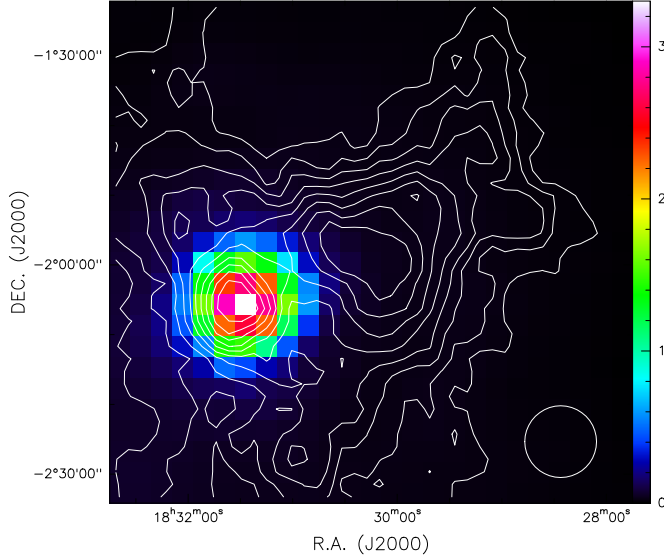


Figure 3. The 6 cm radio continuum distribution superposed on the H_2CO integrated absorption contours toward Aquila MC. The H_2CO contour levels are the same as those in Fig.1. The temperature color bar is given in units of K. The white circle in the lower right illustrates the half-power beam size of $10'$.

or a change in optical depth corresponding to Serpens South in Fig.1b. The velocity distributions of H_2CO is smooth and shows a gradient towards the East of the AMC (Fig.2a). In the W40 region the velocity of ~ 7 km/s corresponds to the systematic velocity of cold gas surrounding the entire region (Shimoikura et al. 2015) and agrees with the velocity found at the periphery of this region by Shimoikura et al. (2018). The velocity of H_2CO (~ 6 km/s) at the southern part of main body of Serpens South agrees with the ^{13}CO velocity distribution. On the other hand, the velocity structure of ^{13}CO (Fig.2b) shows significant substructure and a gradient towards the North-East. The low intensity regions at the boundary between W40 and Serpens South may be related to an interaction between the regions as suggested by Shimoikura et al. (2018). In detail, the H_2CO absorption and ^{13}CO emission display different distributions and there is no clear evidence that the Serpens South region is superposed on the sky with the W40 region.

The 5 GHz radio continuum image within AMC is displayed in Fig.3. The continuum temperature T_c in the H II region ranges from 1 to 3.3 K, and is less than 0.04 K in Serpens South (in Tab.1, col.6). The strong H_2CO absorption at W40 is clearly related to the radio continuum of the H II region, while the continuum is significantly weaker at Serpens South. Because the ^{13}CO emission does not show any enhancement at Serpens South, the H_2CO absorption there should result from an en-

hanced continuum background within Serpens South in addition to the cosmic microwave background (CMB). Therefore the absorption contours in W40 and Serpens South define the extent of the region that is affected by the ongoing star formation, which is well beyond the sites of star formation.

The formaldehyde line is in absorption across the whole region of W40 and Serpens South. This can only happen when everywhere the excitation temperature of the 6-cm line is less than the brightness temperature of the radio continuum sources plus the microwave background. While the excitation temperature T_{ex} may be uniformly low (≤ 1 K) in cold clouds (Heiles 1973), the excitation conditions may vary strongly across star formation regions. Therefore, a simple determination of the absorbing H_2CO column density would not be accurate. Instead we perform an approximate determination of the excitation temperature of H_2CO across the region. Making the imperfect assumption that the column densities of H_2CO and $^{13}CO(1-0)$ are correlated, we may estimate the H_2CO column density from the column density of $^{13}CO(1-0)$, which may be obtained from Sato et al. (1994). Assuming an H_2CO to H_2 abundance ratio of 3×10^{-9} (Evans et al. 1975) and a $^{13}CO(1-0)$ to H_2 abundance ratio of 2.4×10^{-6} (Ripple et al. 2013), the column density ratio of between H_2CO and $^{13}CO(1-0)$ may be calculated as:

$$N(H_2CO) = 1.25 \times 10^{-3} N(^{13}CO). \quad (1)$$

Using the optical depth τ_{app} of H_2CO as calculated using the formulation in Pipenbrink & Wendker (1988):

$$N(H_2CO) = 9.4 \times 10^{13} \cdot \tau_{app} \cdot \Delta V (cm^{-2}), \quad (2)$$

which already assumed a mean value for $T_{ex} = 2$ K. The excitation temperature of H_2CO may then be calculated using Heiles (1973) as follows:

$$T_L = (T_{ex} - T_c)[1 - \exp(-\tau_{app})](K), \quad (3)$$

where T_L is the antenna temperature of the absorption line in degrees kelvin, and T_c is the continuum brightness temperature of the radio background plus the CMB. The results for $N(H_2CO)$ and T_{ex} are presented in Tab.1.

The distribution of T_{ex} determined in this manner shows an enhanced temperature around W40 H II region ranging from 2 - 5 K and around Serpens South ranging from 1 - 2 K (Fig.4). This enhanced T_{ex} in Serpens South confirms the presence of local heating source and ongoing star formation activity. In addition, there is another Serpens 3 region in the formaldehyde absorption structure south of W40 that shows similar conditions of (prestellar) star-formation and inferred weak radio

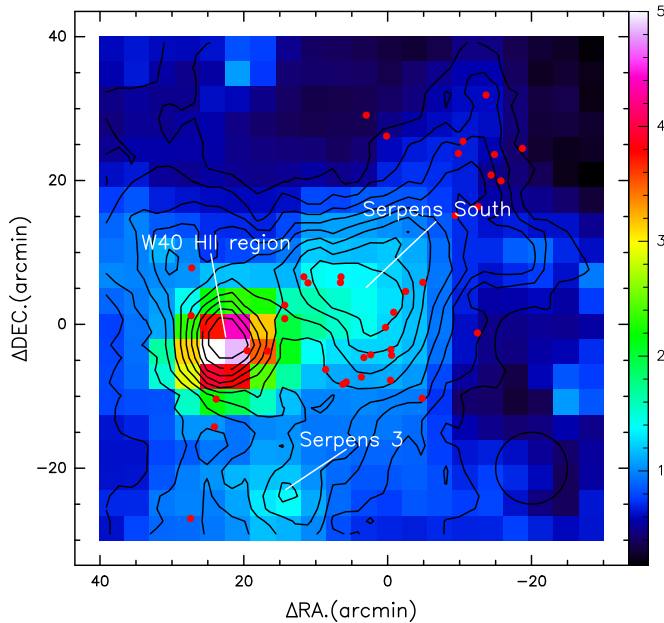


Figure 4. Distribution of T_{ex} of H₂CO absorption line superposed on the integrated absorption contours of H₂CO. The contour levels are the same as Fig.1. The T_{ex} color bar is given in units of K. The black circle in the lower right illustrates the half-power beam size of 10'.

continuum (Fig.4). It appears that the extent of the H₂CO absorption is determined mostly by the excitation of the molecules in regions that are affected by the star formation rather than by the availability of molecular material as represented by the ¹³CO($J = 1 - 0$) distribution. In order to connect the Serpens 3 region with evidence of ongoing star formation, the locations of protostellar cores (Könyves et al. 2015) in the region have been added to Fig. 4. While there are protostellar cores associated with W40 and Serpens South, there are no cores (yet) present around Serpens 3. This would suggest that the Serpens 3 region is still less evolved than the other regions of star-formation. On the other hand, protostellar cores are found around the north-west extension of the H₂CO absorption, which shows less enhancement of T_{ex} but may also qualify as a star-forming region.

The map of the H₂CO line width superposed on the H₂CO integrated intensity contours and spectral plots at four selected regions are shown in Fig.5. The spectra at locations (A) around W40 HII and (B) around Serpens South show a single feature with a multicomponent substructure. The spectral feature at Serpens South is slightly weaker and broader than the feature at W40 and shows shallow redshifted and blueshifted wings, possibly resulting from outflows or the superposition of multiple components. The W40 spectrum shows a possible

blueshifted feature in at -8.5 km s^{-1} that could have a counterpart in the H110 α RL at that location (see section below). The spectra at locations (C) and (D) show a broader multicomponent structure. In the (C) region at a distance of 0.7 pc West of the W40 HII the spectrum is broadened relative to the W40 spectrum (A) and has a low velocity shoulder similar to that found in the ¹³CO($1 - 0$) spectrum and the map of Figure 2b. This lower velocity component may suggest the presence of an outflow component associated with the W40 HII region. The southeastern region (D) of Serpens 3 also shows line broadening toward lower velocities as compared with the spectrum at W40 (A) as well as a high-velocity wing that may result from a superposition of cloud filaments moving to the northeast. In addition, there may be a separate high-velocity component at 15 km s^{-1} .

The H₂CO channel maps are presented in Fig.6 with velocity interval of 1 km s^{-1} . Most of the Serpens South part has a velocity of 6 km s^{-1} , while most of the W40 part has velocity of 7 km s^{-1} . In the 5 km s^{-1} panel an east-west and a southeast-northwest velocity-coherent linear structure are present, which resemble the linear structures in ¹³CO($1 - 0$) intensity map (Fig.1b). Similarly at 8 km s^{-1} there is a northeast-southwest structure running through the W40 region. In order to emphasize these structures, we indicate with dashed curves the locations of apparently velocity-coherent structures superposed on the H₂CO intensity map integrated over the intervals of $5 - 6 \text{ km s}^{-1}$ in Fig.7. Assuming the distance of 436 pc, these linear structures are about $5 - 10 \text{ pc}$ in length and they may be remnants of the super-bubbles converging in our observed area (see also Nakamura et al. (2017)). It should be noted that our three star formation regions coincide with intersection points of these linear structures.

3.2. The H110 α Recombination Line

The H110 α RRL is only detected at the W40 HII region. The spectrum of the H110 α line at W40 is presented in Fig.8 together with the ¹³CO($1 - 0$) profile at the same location. This much broader profile comes from the distribution across the circular image of W40, starting at 10 km s^{-1} and tapering off at -20 km s^{-1} . However, the H110 α spectrum at W40 does not have a counterpart in the ¹³CO($1 - 0$) profile at lower velocities, but there may be weak spectral component (to be confirmed) in the H₂CO absorption spectrum at -8.5 km s^{-1} . With a peak continuum temperature of 3.33 K, the optical depth (T_L/T_c) has a peak value of 0.038, with an average value of 0.15. The profile of the H110 α line resembles a spherical (blueshifted) outflow with an

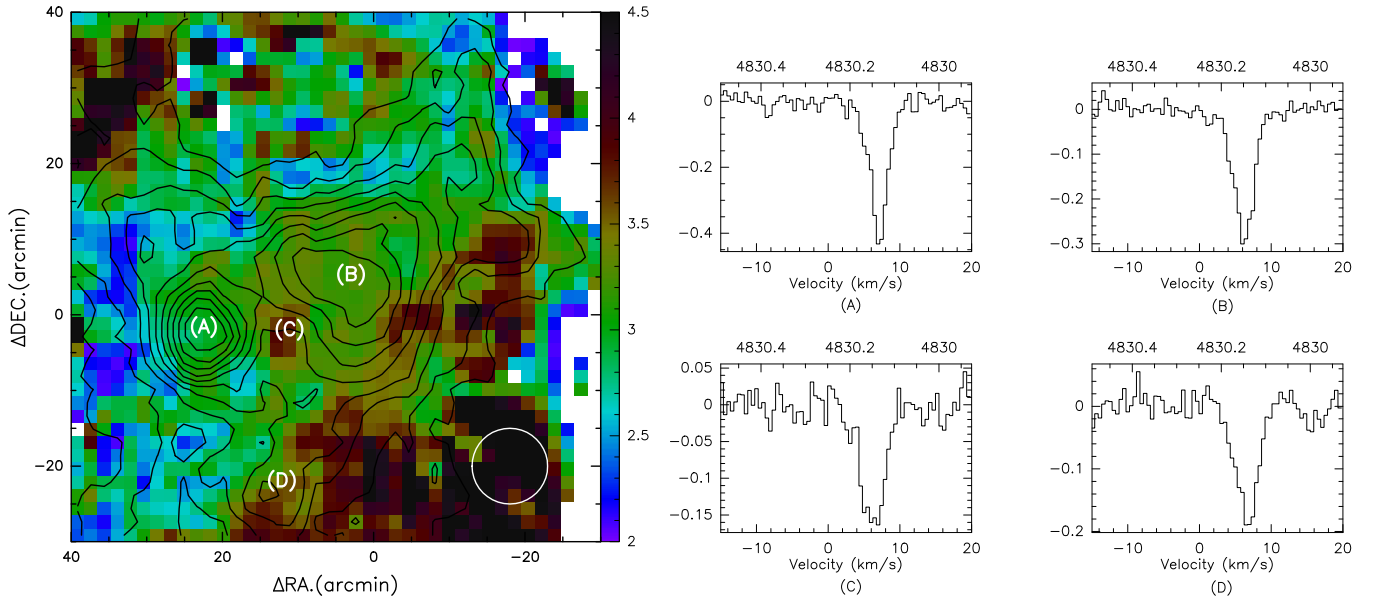


Figure 5. The H_2CO line width map superposed on the H_2CO integrated intensity contours (left panel) and spectra at four selected regions (right panels). The contour levels are the same as Fig.1. The line width color bar is given in units of km s^{-1} . The white circle in the lower right illustrates the half-power beam size of $10'$.

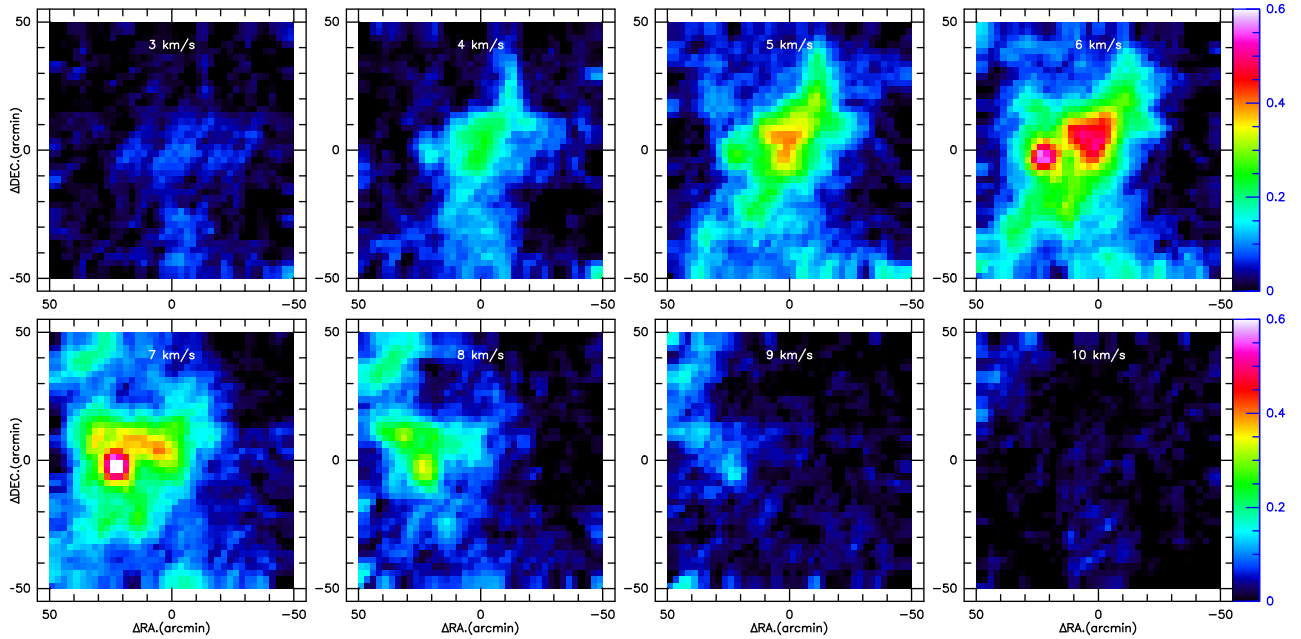


Figure 6. H_2CO velocity channel maps toward the Aquila Molecular Cloud. The color bar is in units of K km s^{-1} .

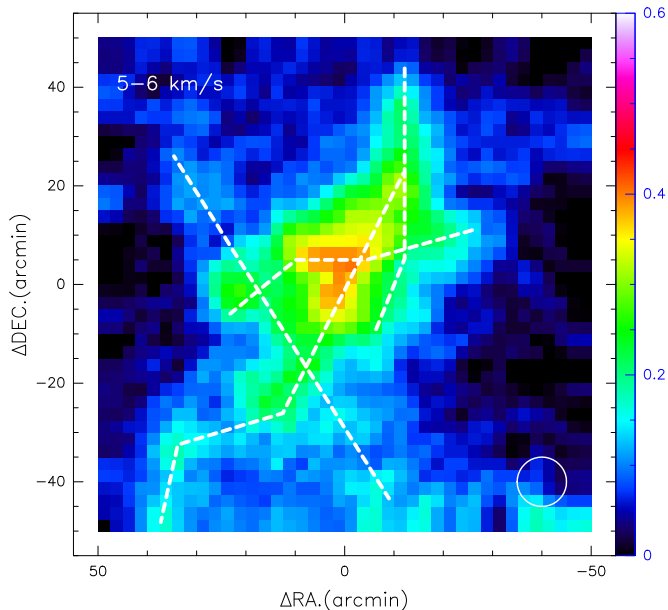


Figure 7. Intensity map of the H₂CO absorption integrated over the velocities of 5 - 6 km s⁻¹. The dashed lines represent filamentary structures that may be discerned in the Aquila Molecular Cloud. The white circle in the lower right illustrates the half-power beam size of 10'.

approximate $(1 - (V/V_o)^2)^n$ shape, where outflow velocity V_o is on the order of 25 km s⁻¹. The local thermodynamic equilibrium electron temperature T_e^* is determined using recombination lines by Brown et al. (1978) discussions as follows:

$$T_e^* = [3.624 \times 10^4 \cdot (T_c / (T_L \cdot \Delta v))]^{0.87}, \quad (4)$$

where the T_e^* indicates a value of 7300 K assuming the peak optical depth and a total line width of 35 km s⁻¹. This value is meaningful when all H110 α emission originates within the outskirts of a typical H II region.

4. CONCLUSION

The H₂CO (1₁₀ - 1₁₁) absorption line and H110 α RRL emission line have been mapped for the first time toward the Aquila molecular cloud containing the W40 H II region and the Serpens South region. The map of the integrated intensity of the H₂CO absorption clearly defines the boundaries of the area that is affected by the embedded star formation. There is prominent absorption at the location of the W40 H II region and weaker absorption in the Serpens South region. A third star formation region Serpens 3 has been identified 1.4 pc south of W40. No substantial correspondence has been found between the three star formation regions and the emission map of ¹³CO(1 - 0). Except for the W40 region, the intensity and velocity distributions of H₂CO and ¹³CO(1 - 0) do not agree well with each other.

The radio continuum structure of the region shows a T_c peak at the W40 H II region, but only estimated values of 0.04 K in the Serpens South region and at Serpens 3. Therefore, the H₂CO absorption at W40 comes from the H II region plus the CMB background, while the weaker components at Serpens South and the Serpens 3 regions result from a weak continuum background plus the CMB. The extent of the H₂CO absorption confirms that it is mostly determined by the excitation of the molecules in regions that are affected by the star formation rather than the availability of molecular gas as depicted by ¹³CO(J = 1 - 0).

Instead of determining the absorbing column density of the formaldehyde across the region with clearly varying environmental conditions, we determined the excitation temperature of the H₂CO. Assuming that the column densities of H₂CO relates to that of ¹³CO(1 - 0) (see Tang et al. (2013)), and that there is fixed abundance ratio of H₂CO and ¹³CO(1 - 0), the column density of ¹³CO(1 - 0) may be used to determine the T_{ex} distribution. While this procedure may not be very reliable, the T_{ex} shows enhancements in the W40 H II region ranging from 2 to 5 K, and > 2 at Serpens South. This also identifies the new star formation region Serpens 3 region with $T_{ex} = 2$ K. The results show that the local conditions strongly affect the excitation of H₂CO and that assuming a constant value for T_{ex} would not be appropriate across this region.

The velocity structure of H₂CO is very smooth while the velocity structure of ¹³CO(1 - 0) has much fine structure and a gradient in a different direction. Therefore, the presence of H₂CO absorption may be correlated with significant substructure within the ¹³CO(1 - 0) integrated emission structure but there is no global correlation. The integrated intensity map of ¹³CO(1 - 0) shows several fine structure regions with discrepant velocities. One of these regions at about 1.2 pc west of W40 has a larger linewidth for H₂CO and shows a lower ¹³CO(1 - 0) velocity. This region may be associated with an outflow found in a near-infrared survey by Zhang et al. (2015).

Some velocity-coherent filamentary structures have been identified in velocity channel maps of H₂CO that are possible remnants of earlier super-bubble structures. Assuming the distance of 436 pc, these linear structures range between about 5 - 10 pc in length. The three star formation regions are found to lie close to intersection points of these filaments, which may suggest a causal relation. The observed velocity substructure of the H₂CO absorption lines may also relate to the presence of such filaments.

The H110 α RRL is only detected in the W40 H II region. The emission spectrum of H110 α shows a broad

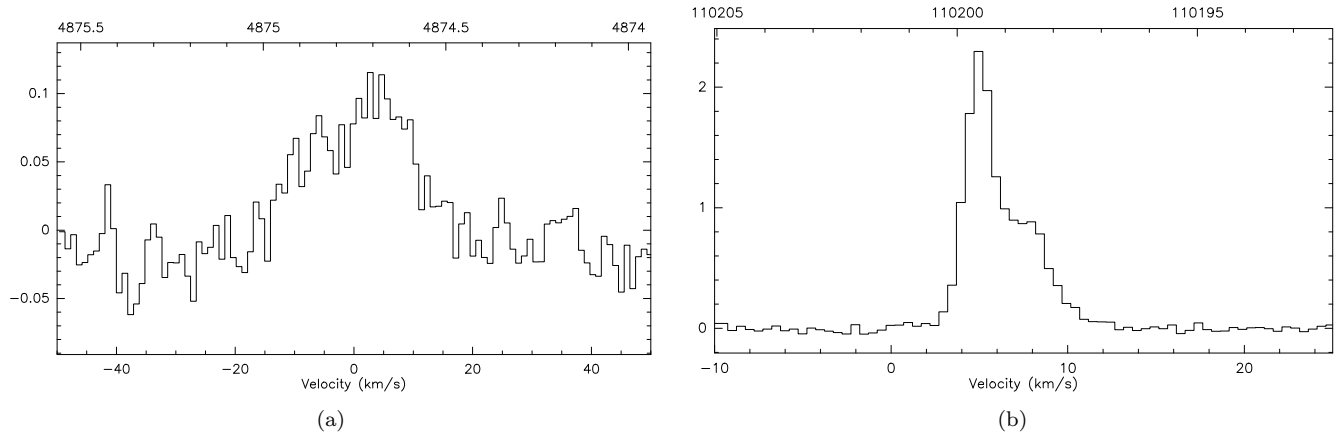


Figure 8. The spectra of (a) the H110a emission and (b) the $^{13}\text{CO}(J = 1 - 0)$ emission at the center of W40 H II region (region A in Fig.5).

profile covering a velocity range of 30 km s^{-1} . The shape of the spectral profile suggests that this emission originates in a shell in front of W40 that is spherically expanding at 26 km s^{-1} . The LTE electron temperature corresponding to the line strength is estimated at 7900 K, which is typical value for the outskirts of an H II region.

Sensitive mapping of H_2CO absorption has been able to correctly identify star-formation activity in complex molecular clouds such as the Aquila Complex. In addition, the detailed structure of the absorption lines may reveal discrepant velocity components resulting from outflow regions.

This work was sponsored by CAS-TWAS President's Fellowship for International Doctoral Students, and The National Natural Science foundation of China under grants 11433008, 11703074, 11703073, and 11603063, and The Program of the Light in China's Western Region (LCRW) under grant Nos. 2016-QNXZ-B-22, 2016-QNXZ-B-23, and 2018-XBQNXZ-B-024. W.A.B. has been funded by Chinese Academy of Sciences President's International Fellowship Initiative under grant No. 2019VMA0040. This work is based on observations made with the Nanshan 25m radio telescope, which is operated by the Kay Laboratory of Radio Astronomy, Chinese Academy of Sciences.

REFERENCES

- Bontemps, S., André, P., Könyves, V., et al. 2010, *A&A*, 518, L85
- Brown, R. L., Lockman, F. J., & Knapp, G. R. 1978, *ARA&A*, 16, 445
- Dame, T. M., Hartmann, D., & Thaddeus, P. 2001, *ApJ*, 547, 792
- Davies, R. D., & Few, R. W. 1979, *The Large-Scale Characteristics of the Galaxy*, ed. W. B. Burton, 81
- Downes, D., Wilson, T. L., Bieging, J., & Wink, J. 1980, *A&AS*, 40, 379
- Evans, N. J., II, Zuckerman, B., Morris, G., & Sato, T. 1975, *ApJ*, 196, 433
- Gutermuth, R. A., Bourke, T. L., Allen, L. E., et al. 2008, *ApJL*, 673, L151
- Heiles, C. 1973, *ApJ*, 183, 441
- Könyves, V., André, P., Men'shchikov, A., et al. 2015, *A&A*, 584, A91
- Nakamura, F., Dobashi, K., Shimoikura, T., Tanaka, T., & Onishi, T. 2017, *ApJ*, 837, 154
- Ortiz-León, G. N., Dzib, S. A., Kounkel, M. A., et al. 2017, *ApJ*, 834, 143
- Pipenbrink, A., & Wendker, H. J. 1988, *A&A*, 191, 313
- Prato, L., Rice, E. L., & Dame, T. M. 2008, *Where are all the Young Stars in Aquila?*, ed. B. Reipurth, 18
- Ripple, F., Heyer, M. H., Gutermuth, R., Snell, R. L., & Brunt, C. M. 2013, *MNRAS*, 431, 1296
- Sato, F., Mizuno, A., Nagahama, T., et al. 1994, *ApJ*, 435, 279
- Shimoikura, T., Dobashi, K., Nakamura, F., Shimajiri, Y., & Sugitani, K. 2018, *PASJ*, arXiv:1809.09855
- Shimoikura, T., Dobashi, K., Nakamura, F., et al. 2015, *ApJ*, 806, 201
- Smith, J., Bentley, A., Castelaz, M., et al. 1985, *ApJ*, 291, 571
- Sun, X. H., Reich, W., Han, J. L., et al. 2011, *A&A*, 527, A74
- Tang, X. D., Esimbek, J., Zhou, J. J., et al. 2013, *A&A*, 551, A28

Vanden Bout, P. A., Snell, R. L., & Wilson, T. L. 1983,
A&A, 118, 337

Young, K. E., Lee, J.-E., Evans, N. J., II, Goldsmith, P. F.,
& Doty, S. D. 2004, ApJ, 614, 252
Zhang, M., Fang, M., Wang, H., et al. 2015, ApJS, 219, 21

Table 1. Parameters of the H₂CO (1₁₀ – 1₁₁) absorption line

Offset	Flux	Velocity	Width	T_L	T_C	τ_{app}	$N(H_2CO)$	T_{ex}
arcmin	K km s ⁻¹	km s ⁻¹	km s ⁻¹	K	K		10 ¹² cm ⁻²	K
(1)	(2)	(3)	(4)	(5)	(6)	(7)	(8)	(9)
-25,-30	-0.2376 (0.02)	7.187 (0.18)	4.517 (0.52)	-0.049	0.011	0.08	3.19	0.69
-15,-30	-0.2935 (0.02)	5.66 (0.24)	5.95 (0.49)	-0.046	0.024	0.08	4.20	0.67
-10,-30	-0.2947 (0.02)	5.898 (0.15)	4.279 (0.33)	-0.065	0.027	0.11	4.40	0.65
-5,-30	-0.3709 (0.02)	5.647 (0.10)	3.853 (0.21)	-0.090	0.029	0.17	6.06	0.62
0,-30	-0.3654 (0.02)	5.883 (0.14)	4.114 (0.28)	-0.083	0.031	0.14	5.54	0.66
5,-30	-0.3531 (0.02)	6.193 (0.12)	3.835 (0.26)	-0.087	0.036	0.15	5.24	0.68
10,-30	-0.45 (0.02)	6.418 (0.11)	4.106 (0.27)	-0.103	0.043	0.12	4.77	0.93
15,-30	-0.5038 (0.03)	6.709 (0.10)	4.065 (0.23)	-0.116	0.046	0.12	4.48	1.09
20,-30	-0.4239 (0.03)	6.345 (0.12)	3.844 (0.27)	-0.104	0.048	0.12	4.16	1
25,-30	-0.3951 (0.03)	6.704 (0.13)	3.851 (0.30)	-0.096	0.051	0.12	4.33	0.91
30,-30	-0.4358 (0.01)	6.626 (0.05)	3.274 (0.11)	-0.125	0.061	0.17	5.20	0.87
35,-30	-0.3491 (0.02)	6.514 (0.07)	2.434 (0.14)	-0.135	0.072	0.2	4.56	0.82
40,-30	-0.2275 (0.02)	6.627 (0.10)	2.412 (0.24)	-0.089	0.075	0.19	4.24	0.59
-15,-25	-0.3384 (0.03)	5.586 (0.26)	6.38 (0.68)	-0.050	0.024	0.07	4.01	0.79
-10,-25	-0.3575 (0.03)	6.19 (0.16)	4.482 (0.36)	-0.075	0.029	0.11	4.58	0.76
-5,-25	-0.4409 (0.02)	5.608 (0.12)	4.842 (0.33)	-0.086	0.032	0.11	5.12	0.84
0,-25	-0.3756 (0.02)	5.548 (0.12)	4.069 (0.28)	-0.087	0.033	0.13	4.83	0.76
5,-25	-0.4196 (0.02)	6.081 (0.09)	3.883 (0.18)	-0.102	0.034	0.14	5.04	0.83
10,-25	-0.5856 (0.02)	6.525 (0.07)	3.599 (0.16)	-0.153	0.043	0.16	5.32	1.09
15,-25	-0.6487 (0.02)	6.611 (0.06)	3.69 (0.14)	-0.165	0.056	0.13	4.48	1.42
20,-25	-0.4641 (0.02)	6.592 (0.07)	3.239 (0.17)	-0.135	0.055	0.14	4.19	1.11
25,-25	-0.387 (0.02)	6.872 (0.07)	2.765 (0.16)	-0.131	0.058	0.16	4.09	0.96
30,-25	-0.4065 (0.02)	6.844 (0.06)	2.742 (0.13)	-0.139	0.067	0.16	4.22	0.99
35,-25	-0.2898 (0.02)	6.742 (0.07)	2.485 (0.15)	-0.110	0.072	0.19	4.52	0.7
-15,-20	-0.2043 (0.02)	6.119 (0.24)	4.444 (0.49)	-0.043	-	0.06	2.44	0.76
-10,-20	-0.2911 (0.02)	6.787 (0.17)	4.375 (0.38)	-0.063	0.032	0.1	4.12	0.69
-5,-20	-0.3486 (0.03)	6.587 (0.16)	4.421 (0.39)	-0.074	0.038	0.09	3.91	0.86
0,-20	-0.3905 (0.03)	6.243 (0.15)	4.351 (0.31)	-0.084	0.033	0.11	4.42	0.86
5,-20	-0.5314 (0.03)	6.276 (0.12)	4.039 (0.31)	-0.124	0.034	0.16	6.17	0.86
10,-20	-0.6238 (0.02)	6.413 (0.07)	3.663 (0.17)	-0.160	0.052	0.18	6.35	1
15,-20	-0.5478 (0.02)	6.644 (0.04)	3.077 (0.10)	-0.167	0.076	0.17	4.82	1.16
20,-20	-0.4843 (0.02)	6.485 (0.06)	2.919 (0.16)	-0.156	0.091	0.16	4.37	1.15
25,-20	-0.416 (0.02)	6.98 (0.07)	2.798 (0.15)	-0.140	0.088	0.16	4.22	1.03
30,-20	-0.3507 (0.02)	6.755 (0.07)	2.573 (0.17)	-0.128	0.085	0.18	4.29	0.87
35,-20	-0.2327 (0.02)	7.052 (0.13)	2.698 (0.36)	-0.081	0.077	0.16	4.06	0.63
40,-20	-0.1936 (0.02)	7.092 (0.16)	2.619 (0.40)	-0.069	0.072	0.13	3.27	0.63
-15,-15	-0.18 (0.02)	5.807 (0.37)	5.28 (0.79)	-0.032	0.021	0.07	3.34	0.51

Table 1 continued

Table 1 (*continued*)

Offset	Flux	Velocity	Width	T_L	T_C	τ_{app}	$N(H_2CO)$	T_{ex}
arcmin	K km s ⁻¹	km s ⁻¹	km s ⁻¹	K	K		10 ¹² cm ⁻²	K
(1)	(2)	(3)	(4)	(5)	(6)	(7)	(8)	(9)
-10,-15	-0.2576 (0.02)	5.85 (0.13)	3.681 (0.33)	-0.066	0.034	0.12	4.08	0.62
-5,-15	-0.3863 (0.02)	5.914 (0.08)	3.561 (0.20)	-0.102	0.039	0.13	4.39	0.87
0,-15	-0.5037 (0.03)	6.333 (0.10)	4.047 (0.26)	-0.117	0.031	0.14	5.26	0.94
5,-15	-0.6316 (0.02)	6.156 (0.06)	3.962 (0.17)	-0.150	0.041	0.18	6.72	0.95
10,-15	-0.6291 (0.02)	6.35 (0.05)	3.592 (0.13)	-0.165	0.070	0.21	7.21	0.93
15,-15	-0.4989 (0.01)	6.824 (0.04)	2.981 (0.11)	-0.157	0.125	0.19	5.25	1.04
20,-15	-0.4105 (0.02)	6.802 (0.07)	2.693 (0.16)	-0.143	0.189	0.25	6.43	0.83
25,-15	-0.3963 (0.02)	6.883 (0.06)	2.811 (0.15)	-0.132	0.168	0.19	4.98	0.94
30,-15	-0.3329 (0.02)	7.104 (0.07)	2.96 (0.19)	-0.106	0.135	0.15	4.15	0.9
40,-15	-0.1788 (0.02)	7.287 (0.21)	3.214 (0.58)	-0.052	0.081	0.1	3.16	0.61
-15,-10	-0.2646 (0.02)	5.313 (0.12)	3.873 (0.33)	-0.064	0.026	0.19	6.81	0.4
-10,-10	-0.3038 (0.02)	5.827 (0.11)	3.162 (0.25)	-0.090	0.035	0.24	7.09	0.46
-5,-10	-0.5445 (0.03)	5.982 (0.08)	3.54 (0.19)	-0.144	0.034	0.18	5.83	0.93
0,-10	-0.6587 (0.02)	6.055 (0.06)	3.713 (0.16)	-0.167	0.036	0.19	6.61	1
5,-10	-0.6776 (0.02)	6.162 (0.06)	3.597 (0.15)	-0.177	0.048	0.2	6.79	1.02
10,-10	-0.6345 (0.03)	6.208 (0.06)	3.215 (0.15)	-0.185	0.105	0.22	6.80	1.02
15,-10	-0.5845 (0.02)	6.538 (0.04)	3.125 (0.12)	-0.176	0.449	0.2	5.84	1.43
20,-10	-0.6362 (0.03)	7.295 (0.06)	3.039 (0.15)	-0.197	1.257	0.27	7.59	2.1
25,-10	-0.5281 (0.03)	7.238 (0.07)	2.84 (0.17)	-0.175	1.093	0.15	4.06	2.33
30,-10	-0.3295 (0.02)	7.465 (0.08)	2.657 (0.20)	-0.116	0.314	0.16	3.89	1.12
35,-10	-0.2776 (0.02)	7.476 (0.10)	2.296 (0.21)	-0.114	0.148	0.19	4.01	0.82
-15,-5	-0.3798 (0.02)	5.355 (0.09)	4.264 (0.27)	-0.084	0.030	0.22	8.69	0.46
-10,-5	-0.45 (0.02)	5.968 (0.07)	3.508 (0.18)	-0.121	0.038	0.22	7.14	0.66
-5,-5	-0.6701 (0.02)	6.133 (0.06)	3.641 (0.16)	-0.173	0.038	0.18	6.21	1.08
0,-5	-0.8745 (0.02)	6.01 (0.04)	3.509 (0.10)	-0.234	0.042	0.22	7.34	1.21
5,-5	-0.8472 (0.02)	6.016 (0.04)	3.376 (0.10)	-0.236	0.065	0.23	7.32	1.21
10,-5	-0.7178 (0.02)	6.341 (0.05)	3.637 (0.13)	-0.185	0.285	0.21	7.03	1.28
15,-5	-0.7391 (0.03)	6.608 (0.06)	3.475 (0.15)	-0.200	1.645	0.37	12.10	2.29
20,-5	-1.097 (0.03)	7.125 (0.05)	3.275 (0.13)	-0.315	3.327	0.29	8.79	4.59
25,-5	-0.9857 (0.02)	7.261 (0.04)	2.95 (0.09)	-0.314	2.591	0.15	4.24	4.8
30,-5	-0.4751 (0.02)	7.251 (0.06)	2.532 (0.15)	-0.176	0.594	0.13	2.99	2.08
35,-5	-0.2984 (0.02)	7.612 (0.09)	2.313 (0.19)	-0.121	0.175	0.18	3.97	0.9
-20,0	-0.271 (0.02)	5.339 (0.14)	4.025 (0.32)	-0.063	0.018	0.13	5.09	0.52
-15,0	-0.3863 (0.02)	5.753 (0.10)	4.431 (0.25)	-0.082	0.031	0.2	8.43	0.48
-10,0	-0.5059 (0.02)	5.647 (0.08)	3.831 (0.19)	-0.124	0.039	0.22	7.90	0.67
-5,0	-0.8185 (0.02)	6.122 (0.05)	3.973 (0.12)	-0.194	0.041	0.19	7.22	1.14
0,0	-1.007 (0.02)	6.216 (0.03)	3.392 (0.07)	-0.279	0.045	0.26	8.21	1.27
5,0	-0.9486 (0.02)	6.4 (0.03)	3.299 (0.08)	-0.270	0.090	0.21	6.59	1.5
10,0	-0.86 (0.03)	6.425 (0.06)	3.757 (0.16)	-0.215	0.391	0.18	6.43	1.68

Table 1 *continued*

Table 1 (continued)

Offset	Flux	Velocity	Width	T_L	T_C	τ_{app}	$N(H_2CO)$	T_{ex}
arcmin	K km s ⁻¹	km s ⁻¹	km s ⁻¹	K	K		10 ¹² cm ⁻²	K
(1)	(2)	(3)	(4)	(5)	(6)	(7)	(8)	(9)
15,0	-0.7699 (0.02)	6.679 (0.04)	3.431 (0.10)	-0.211	1.617	0.47	15.10	2.18
20,0	-1.089 (0.03)	7.051 (0.04)	3.188 (0.11)	-0.321	3.179	0.35	10.40	4.27
25,0	-1.027 (0.02)	7.212 (0.03)	2.994 (0.08)	-0.322	2.477	0.38	10.70	3.5
30,0	-0.5105 (0.02)	7.433 (0.05)	2.619 (0.13)	-0.183	0.593	0.29	7.24	1.31
35,0	-0.3393 (0.02)	7.531 (0.09)	2.574 (0.20)	-0.124	0.134	0.17	4.21	0.91
-25,5	-0.2438 (0.02)	5.342 (0.13)	3.16 (0.27)	-0.072	0.013	0.14	4.03	0.58
-20,5	-0.3443 (0.02)	6.028 (0.11)	3.645 (0.28)	-0.089	0.019	0.15	5.05	0.67
-15,5	-0.408 (0.01)	6.167 (0.06)	3.627 (0.14)	-0.106	0.028	0.21	7.15	0.59
-10,5	-0.5894 (0.02)	5.994 (0.07)	3.658 (0.17)	-0.151	0.039	0.24	8.29	0.74
-5,5	-0.8586 (0.03)	6.065 (0.05)	3.27 (0.12)	-0.247	0.041	0.27	8.18	1.1
0,5	-1.063 (0.02)	6.245 (0.03)	3.331 (0.07)	-0.300	0.048	0.28	8.83	1.27
5,5	-1.102 (0.02)	6.414 (0.03)	3.341 (0.08)	-0.310	0.076	0.26	8.12	1.44
10,5	-1.041 (0.03)	6.566 (0.05)	3.551 (0.11)	-0.276	0.180	0.23	7.69	1.52
15,5	-0.8165 (0.02)	6.92 (0.05)	3.45 (0.11)	-0.222	0.583	0.32	10.50	1.39
20,5	-0.7599 (0.02)	7.199 (0.05)	3.208 (0.12)	-0.223	1.075	0.62	18.70	1.56
25,5	-0.7333 (0.02)	7.22 (0.04)	3.101 (0.10)	-0.222	0.822	0.42	12.30	1.47
30,5	-0.6069 (0.02)	7.577 (0.04)	2.89 (0.11)	-0.197	0.245	0.28	7.50	1.06
35,5	-0.3872 (0.02)	7.632 (0.08)	2.412 (0.18)	-0.151	0.110	0.19	4.36	0.97
-30,10	-0.1847 (0.02)	5.655 (0.15)	2.883 (0.40)	-0.060	0.005	0.11	2.97	0.59
-25,10	-0.3499 (0.02)	5.69 (0.09)	3.304 (0.22)	-0.100	0.013	0.15	4.78	0.71
-20,10	-0.551 (0.03)	5.757 (0.09)	4.103 (0.28)	-0.126	0.017	0.15	5.60	0.95
-15,10	-0.6083 (0.02)	5.947 (0.08)	4.071 (0.21)	-0.140	0.026	0.23	8.66	0.72
-10,10	-0.6509 (0.02)	5.769 (0.05)	3.274 (0.12)	-0.187	0.038	0.31	9.61	0.74
-5,10	-0.879 (0.02)	6.083 (0.04)	3.276 (0.11)	-0.252	0.041	0.28	8.62	1.07
0,10	-0.9472 (0.02)	6.276 (0.04)	3.373 (0.09)	-0.264	0.037	0.26	8.10	1.21
5,10	-0.952 (0.02)	6.468 (0.04)	3.408 (0.11)	-0.262	0.050	0.27	8.52	1.17
10,10	-0.9794 (0.03)	6.587 (0.04)	3.569 (0.11)	-0.258	0.085	0.25	8.47	1.24
15,10	-0.6987 (0.02)	7.048 (0.04)	3.044 (0.09)	-0.216	0.122	0.32	9.19	0.91
20,10	-0.5961 (0.02)	7.577 (0.05)	2.802 (0.12)	-0.200	0.175	0.36	9.56	0.83
25,10	-0.5113 (0.02)	7.537 (0.05)	2.569 (0.12)	-0.187	0.163	0.36	8.81	0.77
30,10	-0.6237 (0.03)	7.788 (0.05)	2.662 (0.14)	-0.220	0.136	0.24	6.08	1.16
35,10	-0.4458 (0.02)	8.229 (0.05)	2.416 (0.12)	-0.173	0.086	0.21	4.86	0.98
-30,15	-7.97E-02(0.01)	5.556 (0.12)	1.537 (0.31)	-0.049	0.005	0.14	1.96	0.39
-25,15	-0.1822 (0.02)	5.638 (0.10)	2.622 (0.31)	-0.065	0.012	0.12	3.02	0.58
-20,15	-0.284 (0.01)	6.01 (0.07)	2.793 (0.16)	-0.096	0.017	0.18	4.72	0.6
-15,15	-0.5231 (0.01)	5.877 (0.04)	3.2 (0.10)	-0.154	0.022	0.31	9.41	0.6
-10,15	-0.6096 (0.01)	5.868 (0.03)	3.21 (0.07)	-0.178	0.031	0.3	9.03	0.72
-5,15	-0.737 (0.02)	6.181 (0.03)	3.195 (0.08)	-0.217	0.036	0.29	8.69	0.9
0,15	-0.7129 (0.02)	6.411 (0.04)	3.166 (0.08)	-0.212	0.033	0.26	7.68	0.96

Table 1 continued

Table 1 (*continued*)

Offset	Flux	Velocity	Width	T_L	T_C	τ_{app}	$N(H_2CO)$	T_{ex}
arcmin	K km s ⁻¹	km s ⁻¹	km s ⁻¹	K	K		10 ¹² cm ⁻²	K
(1)	(2)	(3)	(4)	(5)	(6)	(7)	(8)	(9)
5,15	-0.6118 (0.02)	6.528 (0.05)	3.285 (0.12)	-0.175	0.034	0.2	6.08	1.01
10,15	-0.5221 (0.01)	6.819 (0.04)	3.136 (0.10)	-0.156	0.043	0.18	5.22	1
15,15	-0.4577 (0.02)	6.879 (0.05)	3.173 (0.13)	-0.136	0.059	0.25	7.36	0.68
20,15	-0.4603 (0.02)	7.154 (0.07)	3.133 (0.18)	-0.138	0.077	0.26	7.73	0.68
25,15	-0.5063 (0.01)	7.285 (0.04)	3.016 (0.11)	-0.158	0.077	0.3	8.37	0.7
30,15	-0.5156 (0.02)	7.391 (0.05)	3.025 (0.12)	-0.160	0.061	0.26	7.29	0.77
35,15	-0.473 (0.02)	7.632 (0.06)	3.264 (0.15)	-0.136	0.048	0.16	5.02	0.95
40,15	-0.3587 (0.02)	8.072 (0.08)	2.938 (0.24)	-0.115	0.046	0.16	4.45	0.82
-25,20	-8.56E-02(0.01)	6.378 (0.13)	1.792 (0.27)	-0.045	0.008	0.21	3.58	0.24
-20,20	-0.2295 (0.02)	6.244 (0.08)	2.34 (0.18)	-0.092	0.014	0.25	5.50	0.43
-15,20	-0.4757 (0.01)	6.112 (0.04)	3.012 (0.10)	-0.148	0.019	0.37	10.60	0.49
-10,20	-0.5878 (0.01)	6.006 (0.04)	2.839 (0.08)	-0.195	0.024	0.34	9.13	0.7
-5,20	-0.4776 (0.02)	6.255 (0.06)	2.81 (0.15)	-0.160	0.027	0.26	6.76	0.74
0,20	-0.3976 (0.02)	6.323 (0.06)	2.697 (0.13)	-0.138	0.030	0.22	5.70	0.72
5,20	-0.2805 (0.02)	6.471 (0.08)	2.734 (0.19)	-0.096	0.033	0.23	5.82	0.51
10,20	-0.2812 (0.02)	6.831 (0.08)	2.741 (0.18)	-0.096	0.036	0.2	5.03	0.58
15,20	-0.2583 (0.01)	6.698 (0.09)	2.994 (0.20)	-0.081	0.040	0.18	5.16	0.52
20,20	-0.2941 (0.03)	7.105 (0.14)	3.265 (0.38)	-0.085	0.035	0.2	6.08	0.51
25,20	-0.3525 (0.01)	6.743 (0.06)	2.994 (0.14)	-0.111	0.033	0.23	6.61	0.56
30,20	-0.4116 (0.02)	7.142 (0.06)	3.144 (0.14)	-0.123	0.029	0.29	8.67	0.51
35,20	-0.3966 (0.02)	7.617 (0.10)	3.869 (0.28)	-0.096	0.028	0.16	5.73	0.69
-25,25	-0.119 (0.02)	6.228 (0.14)	2.038 (0.34)	-0.055	0.007	0.27	5.21	0.24
-20,25	-0.1881 (0.02)	6.228 (0.10)	2.128 (0.20)	-0.083	0.012	0.31	6.26	0.32
-15,25	-0.4305 (0.02)	6.056 (0.05)	3.147 (0.13)	-0.129	0.017	0.26	7.81	0.57
-10,25	-0.4385 (0.02)	5.88 (0.05)	2.623 (0.13)	-0.157	0.022	0.27	6.73	0.68
-5,25	-0.346 (0.02)	6.456 (0.09)	2.854 (0.19)	-0.114	0.023	0.19	5.17	0.67
0,25	-0.2902 (0.02)	6.753 (0.11)	3.032 (0.25)	-0.090	0.028	0.18	5.04	0.58
5,25	-0.1657 (0.02)	6.667 (0.15)	2.502 (0.28)	-0.062	0.031	0.2	4.67	0.38
10,25	-0.1609 (0.02)	6.448 (0.12)	2.629 (0.29)	-0.058	0.033	0.16	3.91	0.43
15,25	-0.1681 (0.02)	6.763 (0.14)	2.926 (0.31)	-0.054	0.034	0.14	3.80	0.45
25,25	-0.283 (0.02)	6.627 (0.12)	3.526 (0.30)	-0.075	0.031	0.15	5.12	0.56
30,25	-0.3594 (0.03)	7.174 (0.14)	3.741 (0.35)	-0.090	0.029	0.19	6.67	0.55
-30,30	-6.26E-02(0.01)	5.851 (0.12)	1.312 (0.26)	-0.045	-	0.29	3.53	0.18
-25,30	-0.1724 (0.03)	6.01 (0.24)	3.71 (0.80)	-0.044	0.004	0.13	4.58	0.36
-20,30	-0.1762 (0.02)	6.304 (0.08)	1.821 (0.18)	-0.091	0.010	0.31	5.39	0.35
-15,30	-0.3506 (0.02)	6.004 (0.07)	2.822 (0.16)	-0.117	0.015	0.22	5.86	0.61
-10,30	-0.3671 (0.02)	5.999 (0.07)	2.835 (0.15)	-0.122	0.016	0.22	5.90	0.63
-5,30	-0.2804 (0.02)	6.453 (0.10)	2.913 (0.18)	-0.090	0.017	0.2	5.54	0.51
0,30	-0.2279 (0.02)	6.54 (0.14)	3.179 (0.28)	-0.067	0.020	0.18	5.48	0.42

Table 1 *continued*

Table 1 (*continued*)

Offset	Flux	Velocity	Width	T_L	T_C	τ_{app}	$N(H_2CO)$	T_{ex}
arcmin	K km s ⁻¹	km s ⁻¹	km s ⁻¹	K	K		10 ¹² cm ⁻²	K
(1)	(2)	(3)	(4)	(5)	(6)	(7)	(8)	(9)
5,30	-0.1997 (0.02)	6.763 (0.16)	2.979 (0.32)	-0.063	0.024	0.21	5.91	0.35
15,30	-0.1365 (0.02)	6.272 (0.19)	3.002 (0.41)	-0.043	0.027	0.12	3.43	0.4
20,30	-0.1653 (0.02)	6.296 (0.21)	3.424 (0.45)	-0.045	0.033	0.1	3.27	0.5
25,30	-0.2251 (0.02)	7.235 (0.14)	2.851 (0.32)	-0.074	0.036	0.15	3.96	0.58
30,30	-0.2934 (0.03)	7.528 (0.20)	4.416 (0.42)	-0.062	0.032	0.15	6.15	0.49
35,30	-0.3368 (0.03)	8.223 (0.21)	4.904 (0.69)	-0.065	0.018	0.14	6.47	0.51
40,30	-0.3056 (0.02)	8.698 (0.12)	3.06 (0.30)	-0.094	0.011	0.25	7.23	0.43
-20,35	-0.122 (0.01)	5.89 (0.11)	2.093 (0.23)	-0.055	0.006	0.24	4.66	0.27
-15,35	-0.3171 (0.02)	6.122 (0.09)	2.985 (0.25)	-0.100	0.009	0.2	5.66	0.56
-10,35	-0.3227 (0.01)	5.761 (0.06)	2.538 (0.13)	-0.119	0.011	0.25	5.88	0.56
-5,35	-0.2316 (0.02)	6.217 (0.13)	3.267 (0.25)	-0.067	0.013	0.16	5.02	0.45
5,35	-0.2155 (0.02)	6.965 (0.14)	3.321 (0.33)	-0.061	0.016	0.16	5.06	0.42
15,35	-0.1827 (0.02)	6.697 (0.17)	3.237 (0.42)	-0.053	0.017	0.12	3.65	0.49
20,35	-0.3746 (0.05)	6.711 (0.53)	9.407 (1.95)	-0.037	-	0.04	3.10	1.08
25,35	-0.2111 (0.02)	7.523 (0.18)	3.495 (0.43)	-0.057	0.022	0.12	4.03	0.51
30,35	-0.2988 (0.02)	7.231 (0.15)	3.975 (0.32)	-0.071	0.019	0.15	5.56	0.53
35,35	-0.4561 (0.02)	7.969 (0.09)	3.785 (0.25)	-0.113	0.011	0.19	6.74	0.67
40,35	-0.4512 (0.03)	8.458 (0.11)	3.865 (0.29)	-0.110	0.010	0.23	8.49	0.54
-15,40	-0.1673 (0.02)	6.02 (0.12)	2.456 (0.30)	-0.064	0.004	0.16	3.79	0.43
-10,40	-0.241 (0.01)	5.977 (0.08)	2.744 (0.18)	-0.083	0.007	0.22	5.59	0.43
5,40	-0.1615 (0.02)	6.872 (0.19)	3.201 (0.45)	-0.047	0.012	0.15	4.46	0.36
10,40	-0.1639 (0.02)	7.148 (0.15)	2.775 (0.31)	-0.056	0.011	0.16	4.14	0.39
15,40	-0.2213 (0.01)	7.189 (0.11)	3.474 (0.26)	-0.060	0.012	0.11	3.73	0.57
20,40	-0.3022 (0.02)	6.847 (0.16)	4.046 (0.40)	-0.070	0.014	0.09	3.45	0.82
25,40	-0.2829 (0.02)	7.331 (0.12)	3.435 (0.29)	-0.077	0.013	0.13	4.10	0.66
30,40	-0.3546 (0.02)	7.693 (0.07)	3.17 (0.17)	-0.105	0.011	0.19	5.71	0.61
35,40	-0.4666 (0.03)	8.02 (0.09)	3.417 (0.26)	-0.128	0.011	0.22	7.06	0.66
40,40	-0.3529 (0.02)	7.929 (0.09)	3.038 (0.25)	-0.109	0.012	0.2	5.76	0.61

NOTE—The central position is 18:30:03 -2:02:40 (EQ J2000).